Research Article | Vol. 10, No. 10 / 1 October 2019 / Biomedical Optics Express 5385

Biomedical Optics EXPRESS

Ratiometric widefield imaging with spectrally balanced detection

SHIMON YUDOVICH,[1] LIOR SHANI,[1] ASAF GRUPI,[1] OMRI BAR-ELLI,[4] DAN STEINITZ,[4] DAN ORON,[4] AND SHIMON WEISS[1,2,3,*]

[1] *Department of Physics, Institute for Nanotechnology and Advanced Materials, Bar-Ilan University, Ramat-Gan, 52900, Israel*
[2] *Department of Chemistry and Biochemistry, University of California Los Angeles, Los Angeles, CA 90095, USA*
[3] *California NanoSystems Institute, University of California Los Angeles, Los Angeles, CA 90095, USA*
[4] *Department of Physics of Complex Systems, The Weizmann Institute of Science, Rehovot 76100, Israel*
[*] *sweiss@chem.ucla.edu*

Abstract: Ratiometric imaging is an invaluable tool for quantitative microscopy, allowing for robust detection of FRET, anisotropy, and spectral shifts of nano-scale optical probes in response to local physical and chemical variations such as local pH, ion composition, and electric potential. In this paper, we propose and demonstrate a scheme for widefield ratiometric imaging that allows for continuous tuning of the cutoff wavelength between its two spectral channels. This scheme is based on angle-tuning the image splitting dichroic beamsplitter, similar to previous works on tunable interference filters. This configuration allows for ratiometric imaging of spectrally heterogeneous samples, which require spectral tunability of the detection path in order to achieve good spectrally balanced ratiometric detection.

© 2019 Optical Society of America under the terms of the OSA Open Access Publishing Agreement

1. Introduction

The image in conventional fluorescence microscopy, where one images the emission intensity of fluorescent molecules or particles, is usually linearly correlated with fluorophore concentration, excitation source intensity, and its environment-dependent quantum yield. In contrast, ratiometric imaging is based on the detection of changes in fluorescence spectra, and is immune to artifacts associated with imaging merely the total emission intensity. Ratiometric fluorescence imaging can be done with either two spectral excitation channels (the sample is successively excited by two wavelengths, and the ratio of the detected emission intensities is calculated), two spectral emission channels (the sample is excited by a single wavelength, and the ratio is calculated using the intensities at two emission-separated spectral regions), or a combination of both [1,2].

Ratiometric fluorescence imaging is commonly used for measurements of single molecule FRET [3,4], single molecule anisotropy [4,5], variations in calcium ion concentrations [6], pH levels [7], solvent polarity [8], and membrane potentials [9] in biological samples. The emission spectra of certain fluorescent probes undergo an environmental parameter-dependent wavelength shift, thus allowing for the quantification of such a parameter by ratiometric detection. Even for indicators that only undergo quenching in the presence of the environmental parameter, but no spectral shifts, such as quinolinium-based chloride indicators, it is possible to synthesize a ratiometric probe by conjugating Cl^--sensitive and -insensitive chromophores [10].

In this paper, we propose and demonstrate the use of an angle-tuned dichroic beamsplitter for ratiometric widefield imaging. The proposed optical set-up, which can be easily implemented for any conventional microscope, provides a versatile and robust solution for performing ratiometric imaging for spectrally heterogeneous samples.

#370784 https://doi.org/10.1364/BOE.10.005385
Journal © 2019 Received 24 Jun 2019; revised 12 Aug 2019; accepted 29 Aug 2019; published 30 Sep 2019

Biomedical Optics EXPRESS

Thin-film interference filters, fabricated by depositing multiple transparent thin-films on an optical substrate, are frequently used in optical instruments for spectral separation and filtering. Since each layer has a different dielectric constant, light will be transmitted and reflected by each layer, resulting in an overall transmission that is highly dependent upon the incident wavelength and the multilayer design [11,12]. A filter design is described by the multilayer composition, the combination of multilayers, and the spacer layers in-between [11]. Depending on the design, interference filters can function as shortpass, longpass, single or multi bandpass filters, with various edge steepness and transmission efficiencies.

When light is incident upon an interference filter at an angle other than normal incidence, the optical path it travels is altered and hence the transmission spectrum modified. For a given transmission spectrum at normal angle of incidence, a spectral feature at wavelength λ_0 of the transmission spectrum will be shifted to a wavelength $\lambda(\theta)$, which can be approximated as $\lambda(\theta) = \lambda_0\sqrt{1-(\sin\theta/n_{eff})^2}$, where θ is the angle of incidence of the collimated light in air, and n_{eff} is the effective index of refraction, which depends upon the multilayer design, and, in general, upon the angle of incidence and polarization [12]. Angle-tuning of thin-film interference filters has become a standard and affordable solution for achieving flexibility in bandpass spectral filtering, while maintaining high transmission efficiency at the relevant spectral regions. Such systems are very suitable for hyperspectral fluorescence microscopy [13] and optical telecommunication networks [14]. In this paper, we extend the concept of angle-tuning for dichroic beamsplitters in a dual-view configuration for ratiometric imaging across an entire field-of-view. The proposed optical set-up enables to optimize the balance of the two channels in ratiometric widefield imaging, which provides a platform for high-speed quantitative imaging with optimal signal detection.

2. Set-up

A key requirement from such a wavelength-tunable ratiometric system is that the image remains unaltered while tuning the cutoff wavelength. In order for the reflected image to maintain its position on the camera while angle-tuning, the image splitting dichroic beamsplitter is placed in a retro-reflector configuration with an additional mirror (Fig. 1), similar to the confocal configuration in reference [15]. Imaging is performed with an inverted widefield microscope (IX73, Olympus), with the image passing through a dichroic beamsplitter and an additional silver mirror placed on a motorized rotation stage (PRMTZ8, Thorlabs), with the rotation axis being the intersection of the two reflecting surfaces, resulting in a retroreflector configuration. The reflected image is then reflected by an additional mirror mounted on a motorized kinematic mount (KS1-Z8, Thorlabs), adjusting any small misalignments that result from a non-ideal retroreflector arrangement. A look-up table is constructed based on detailed characterization of these misalignments. The look-up table allows us to implement automatic spectral tuning of the dichroic and correction of the misalignments, thus maintaining aligned dual-view imaging of the two spectral halves (transmitted and reflected images) for each cutoff setting. We note that these alignment corrections can, in principle, also be performed electronically in a post-processing step. The transmitted and reflected images are directed to two CMOS cameras (ORCA-Flash4.0 V3, Hamamatsu). During imaging, the dichroic is automatically tuned using the motorized components, controlled by software (LabVIEW, National Instruments). When changing the dichroic beamsplitter, a short calibration routine of the motorized components is performed in order to ensure perfect alignment of the reflected beam.

We tested angle-tuning of two commercial dichroic filters: (i) a 594 nm longpass dichroic beamsplitter (Di03-R594, Semrock), and (ii) a 628 nm tunable longpass filter (TLP01-628, Semrock).

Biomedical Optics EXPRESS

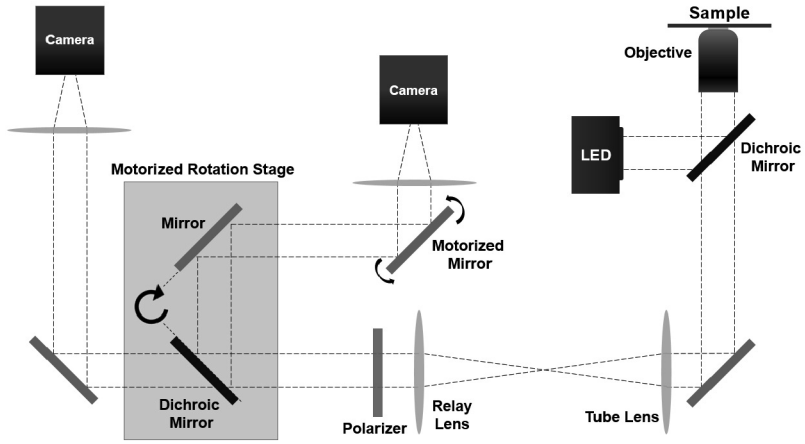

Fig. 1. Optical set-up for spectrally balanced ratiometric widefield imaging. The image is split by a dichroic beamsplitter placed on a motorized rotation stage. The rotation stage holds both the image splitting dichroic beamsplitter, and a silver mirror, thus the dichroic-mirror pair act as a retroreflector, allowing for angle-tuning the dichroic beamsplitter without considerable misalignment of the reflected image.

The transmission spectra of the two angle-tuned dichroic edge filters are shown in Fig. 2(a). Transmission spectra were measured with a spectrometer (USB4000, Ocean Optics) coupled to a multimode fiber (QP600-2-SR, Ocean Optics), positioned at the optical axis after the dichroic beamsplitter, using an unpolarized halogen lamp (U-LH100L-3, Olympus) as the illumination source. We examined the reflected image by imaging <100 nm fluorescent beads (FP-00558-2, Spherotech). For dichroic beamsplitter (i), we observed no significant broadening of the optical point spread function in the reflected image relative to the transmitted image. However, we note that even though the commercial tunable filter (ii) is flat enough for most imaging purposes, it is essentially composed of two longpass filters compensating each other at different angles of incidence. Hence, the reflected image is composed of two spatially separated images, having different spectral components, that combine into a final image at the camera plane. This feature results from the optimized thin-film design of the tunable filter (ii), which is designed to work as a transmission filter, and has negligible effect as long as it is not used for localization microscopy.

The edge cutoff wavelength λ_{DC} and width σ_{DC} are calculated by fitting the transmission curve to a shifted sigmoid function $1/(1+\exp(-(\lambda-\lambda_{DC})/\sigma_{DC}))$, and shown in Fig. 2(b) and 2(c), respectively. Tuning the dichroic beamsplitter around a 45° angle of incidence, the cutoff wavelength shifts approximately linearly with angle for both tuning directions. Though the cutoff wavelength can be continuously tuned, the obtained spectral separation between the two detection channels is restricted by the edge width. Since the incident beam is unpolarized, the edge width of dichroic beamsplitter (i) widens upon tuning the filter at larger angles. This edge widening is mainly the result of polarization splitting at large angles of incidence, which is common for thin-film interference filters [12]. In contrast, the tunable filter (ii), which is designed for angle-tuning, shows minimal polarization splitting, and hence minimal edge widening. Figure 3 demonstrates widefield imaging with spectral tuning of the fluorescence emission from colloidal quantum dots by angle-tuning the dichroic beamsplitter.

We note that points at the sample plane that are at distance L away from the optical axis will diverge after the relay lens at an angle given by $\theta = \arctan(M \times L/f_{relay})$ under the paraxial approximation, where M is the system magnification, and f_{relay} is the focal length of the relay lens. This divergence results in weak variations of the cutoff wavelength across the imaging

Biomedical Optics EXPRESS

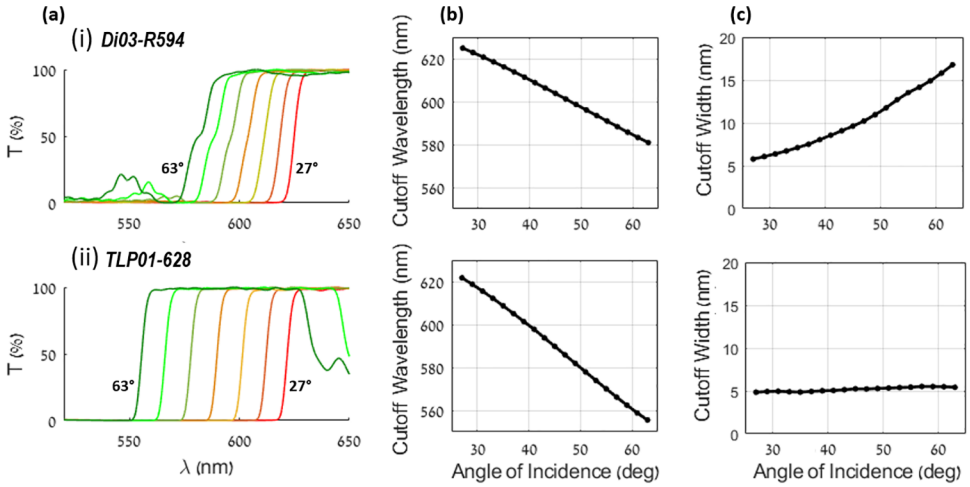

Fig. 2. Transmission spectra characterization of two commercial filters: (i) Di03-R594 (Semrock), a longpass dichroic beamsplitter, and (ii) TLP01-628 (Semrock), a tunable longpass filter. **(a)** shows the transmission spectra of the filters at different angles of incidence. **(b)** and **(c)** show the cutoff wavelength and edge width vs. the angle of incidence, respectively. Since the dichroic beamsplitter (i) is designed to work optimally at 45° angle of incidence, as opposed to the angle-tunable filter (ii), considerable polarization splitting and additional transmission bands near the cutoff wavelength appear when tuning the dichroic beamsplitter to higher angles of incidence.

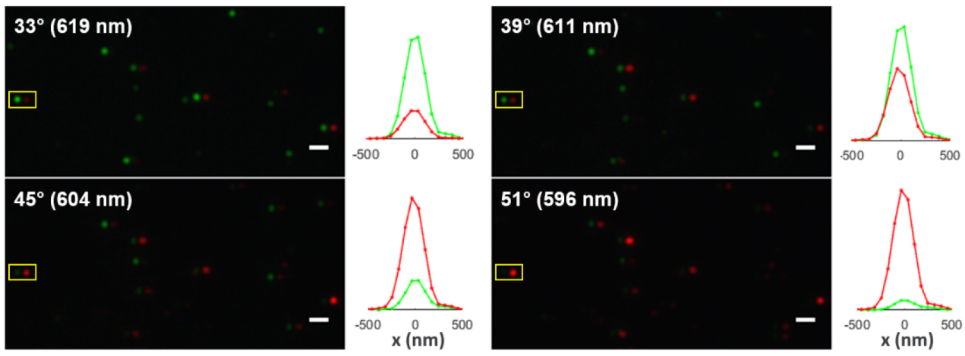

Fig. 3. Widefield fluorescence imaging of quantum dots at different angles of incidence (cutoff wavelengths) of the dichroic beamsplitter. CdSe/ZnS quantum dots (QSP-600, Ocean Nanotech) were diluted and dispersed on a glass coverslip, and imaged with an 100x objective (UPLSAPO100XO, Olympus) while angle-tuning dichroic beamsplitter (i). Images from the two cameras were superimposed into a single image with a small displacement, and false colored with red and green to distinguish between the transmitted and reflected channels, respectively. At the right of each image is the one-pixel line cross section for an individual particle, indicated by the yellow box, at both spectral channels, illustrating tuning of the spectral splitting between the two cameras. Scale bar: 1 µm.

region at the sample plane. For example, assuming the calibration curve (Fig. 2(b)) of the tunable filter (ii), for an optical set-up with an 100X magnification and a $f_{relay} = 180\,mm$ relay lens, the difference between the cutoff wavelength of an imaged point at the optical axis of the objective and a point 50 µm away from it at the sample plane will be approximately 3 nm.

Biomedical Optics EXPRESS

We define the ratiometric value between the two spectral channels as $R = \frac{F_R - F_T}{F_R + F_T}$, with F being the measured intensity at the transmitted/reflected channel. We note that this definition of the spectral ratiometric value is known as the generalized polarization, in analogy to the ratiometric value used in anisotropy measurements [16,17]. In addition, using a standard sample with fixed spectral properties, one can introduce a compensation factor to correct the measured radiometric value for spectral biases in the detection efficiency of the two spectral channels [18]. By approximating the transmission spectrum of a dichroic edge filter as a shifted sigmoid function with a cutoff wavelength λ_{DC} and width σ_{DC}, and assuming an emission spectrum with a Gaussian profile, the transmitted and reflected channel intensities are:

$$F_T = \exp\left[-\left(\frac{\lambda - \lambda_0}{2\sigma}\right)^2\right] \times \left(1 + \exp\left[-\left(\frac{\lambda - \lambda_{DC}}{\sigma_{DC}}\right)\right]\right)^{-1}, \tag{1}$$

$$F_R = \exp\left[-\left(\frac{\lambda - \lambda_0}{2\sigma}\right)^2\right] \times \left(1 + \exp\left[\left(\frac{\lambda - \lambda_{DC}}{\sigma_{DC}}\right)\right]\right)^{-1}, \tag{2}$$

where λ_0 and σ are the emission spectra peak wavelength and width, respectively. The difference of the ratiometric value between spectral states of a fluorophore $\Delta R = R_2 - R_1$, is highly dependent upon the properties of the dichroic filter used for separating the two spectral channels. Figure 4 demonstrates the theoretical dependence of the ratiometric difference ΔR upon changing the edge filter cutoff wavelength and width.

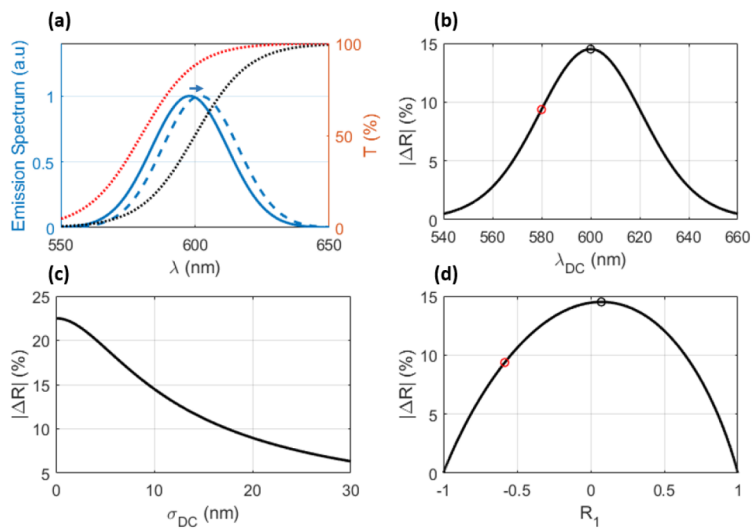

Fig. 4. Theoretical ratiometric shift dependence upon the dichroic edge filter. Assuming a $\sigma = 10\,nm$ emission spectrum width which shifts its peak from 598 nm to 602 nm, as shown in **(a)**, we use equations (1–2) to calculate the ratiometric shift ΔR as function of **(b)** the edge filter cutoff wavelength (assuming a constant edge width of $\sigma_{DC} = 10\,nm$), and **(c)** the dichroic edge width σ_{DC} (assuming a constant edge cutoff wavelength of $\lambda_{DC} = 600\,nm$). Figure **(d)** is an alternative representation of figure **(b)**, in which we convert the cutoff wavelength to the ratiometric value of the initial spectral state. The corresponding values of two specific cutoff wavelengths, 600 nm (black) and 580 nm (red), are shown in figures **(a)**, and **(b, d).**

Biomedical Optics EXPRESS

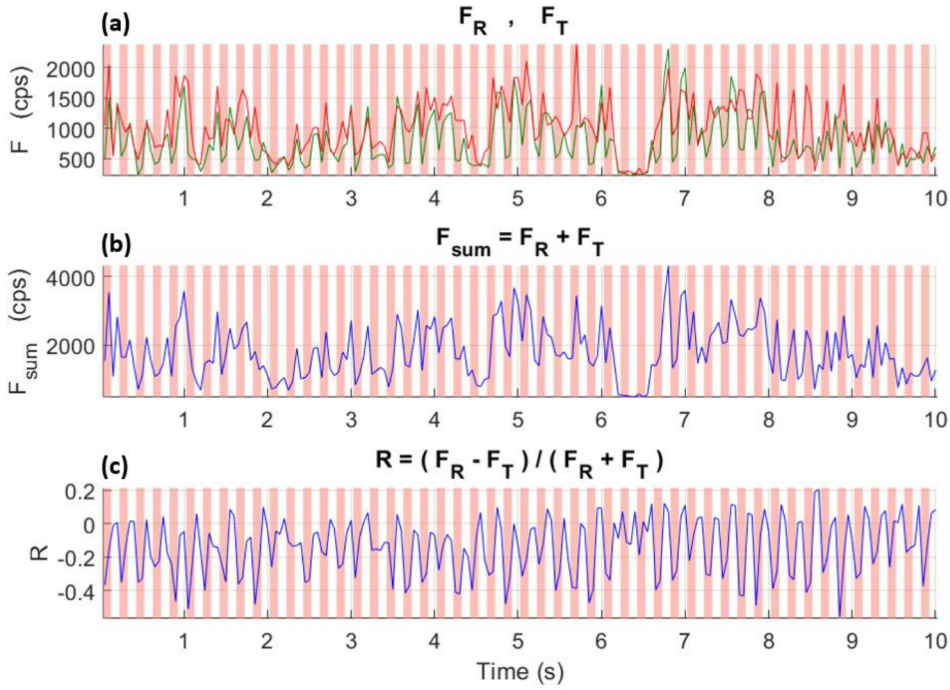

Fig. 5. Ratiometric measurement of QCSE in a semiconductor nanorod. **(a)** The emission fluorescence of a single nanorod under a square wave modulated electric field (f = 5 Hz; E_{max}=300 kV/cm). The cameras were recording at a 20 Hz frame rate, and synchronized to the applied field. Red-shaded areas correspond to E_{max} periods, and white areas indicate zero field. The emission intensity was spectrally split by angle-tuning the dichroic beamsplitter (i), providing a spectrally-balanced detection between the transmitted image (red line) and reflected image (green line). **(b)** and **(c)** show the total emission intensity and ratiometric value between the two channels, respectively. Although there is correlation between the total fluorescence emission intensity and the applied voltage, the spectral shift due to QCSE is clearly demonstrated along the whole trace via the ratiometric measurement.

3. Experimental application

In order to demonstrate the utility of a tunable dichroic beamsplitter for ratiometric imaging, we show two examples of imaging spectral changes of fluorescence emission in response to environmental changes: (a) spectral shift of semiconductor nanocrystals due to the quantum confined Stark effect (QCSE) [19], and (b) spectral response of the voltage sensitive membrane dye di-8-ANEPPS to alternating transmembrane potential in live cells.

As opposed to fluorescent molecules, synthesis of semiconductor nanocrystals produces a heterogeneous sample, and ratiometric imaging may be limited by the available dichroic beamsplitter and sample emission spectrum heterogeneity. The optical scheme proposed here is highly suitable for such experiments, and may be easily implemented in conventional microscopes. Following reference [19], we fabricated interdigitated gold microelectrodes with a 3 µm gap on glass coverslips, and drop-casted a diluted solution of ZnSe/CdS seeded nanorods in order to get single particles in-between the electrodes. A DAQ device (USB-6211, National Instruments) was used to synchronize the two CMOS cameras and the voltage between the microelectrodes, which were connected to a high-voltage amplifier (A-301, A. A. Lab Systems). We note that other processes, beside QCSE, such as Auger recombination and charging, could also contribute

Biomedical Optics EXPRESS

to the signal. Figure 5 shows the fluorescent response of a single nanorod exhibiting QCSE, and illustrates the advantage of a well spectrally-balanced ratiometric detection.

As a second demonstration, we show ratiometric imaging of di-8-ANEPPS, a voltage sensitive membrane dye [20], while inducing a transmembrane voltage with platinum electrodes [21,22]. HEK 293 cells were incubated for one hour on chambered cover glass (C8-1.5H-N, Cellvis) coated with poly-D-lysine (Sigma), allowing the cells to adhere to the glass while still remaining in a spherical shape. The spherical cell geometry provides simplicity, since the induced transmembrane voltage along the great circle parallel to the field of a spherical cell in a homogenous electric field varies as a cosine function [23]. The cells were stained with 10 µM di-8-ANEPPS (Biotium) in a buffer solution (140 mM NaCl, 2.8 mM KCl, 2 mM $CaCl_2$, 2 mM $MgCl_2$, 10 mM glucose, 10 mM HEPES buffer pH 7.4) containing 0.05% pluronic F-127 (Sigma) for 10 minutes in 4°C, and then washed two times. Finally, fresh buffer solution was added and two platinum electrodes 4 mm apart were placed at the edges of the chamber. By angle-tuning filter (ii), we were able to continuously adjust the spectral splitting of di-8-ANEPPS fluorescence emission between the two cameras, as shown in Fig. 6(a).

Using the same electrical amplification and synchronization system as described above, we applied a series of ten 80 V pulses, each 100 ms in duration, with one second between each pulse. Excitation with LEDs (SPECTRA X, Lumencor) was performed stroboscopically only during camera exposure times, in order to avoid unnecessary photobleaching. Upon the application of an electric field, half of the spherical cell membrane polarizes, and the other half depolarizes. Figures 6(b)–6(d) show the fluorescence response of di-8-ANEPPS upon externally applied fields at different imaging conditions. We note that photobleaching is wavelength dependent, hence the signal in different spectral regions decreases at a slightly different rate [24]. In addition, the absorption spectrum of many ratiometric dyes, including ANEPPS dyes, will be dependent upon the variation of the environmental parameter. Therefore, the response of the emission intensity and spectrum will also depend upon the choice of the excitation wavelength [25]. Figures 6(b) and 6(c) show angle-tuning of filter (ii) under 470 nm excitation. For 470 nm excitation, it is mainly the transmitted (red) portion of the emission spectrum that changes upon membrane polarization. However, upon 440 nm excitation, the total detected fluorescence emission is almost unaffected by the electric field (Fig. 6(d), middle panel), while the emission spectrum does shift, and variations due to the applied electric field occur at both detection channels, as seen by the ratiometric curve (Fig. 6(d), bottom panel).

Biomedical Optics EXPRESS

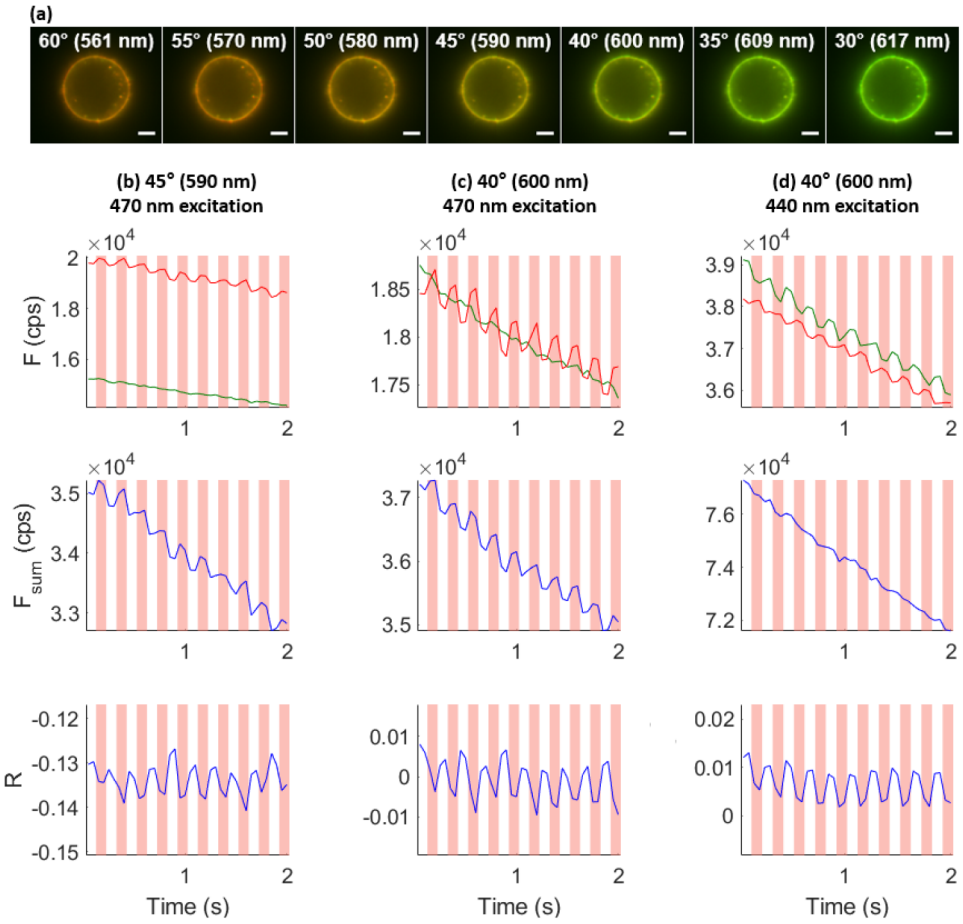

Fig. 6. Ratiometric imaging of HEK 293 cells stained with di-8-ANEPPS upon pulsed electric polarization. **(a)** Ratiometric images of a stained HEK 293 cell at different angles of incidence (cutoff wavelengths) of the tunable filter (ii). Imaging was performed with a 60x objective (PLAPON60XO, Olympus). Images from the two cameras were superimposed into a single image, and false colored with red and green corresponding to the transmitted and reflected channels, respectively. Scale bar: 5 µm. The cells were placed between platinum electrodes and ten pulses of 80 V, each 100 ms in duration, were applied every one second. Three imaging conditions are shown: **(b)** and **(c)** were performed under 470 nm excitation at 45° (590 nm) and 40° (600 nm) angles of incidence, respectively, and **(d)** was performed under 440 nm excitation at 40° (600 nm) angle of incidence. The cameras were recording at a 20 Hz frame rate, and synchronized to the applied field. Red-shaded areas correspond to durations in which the external field was applied, and white areas indicate a duration of 100 ms before each pulse, in which no electric field was applied. The top panel of **(b-d)** show the total detected fluorescence emission from the half of the cell closer to the positive electrode, for both the transmitted (red line) and reflected (green line) images. The middle and bottom panels of **(b-d)** show the total emission intensity and ratiometric value between the two channels, respectively.

Biomedical Optics EXPRESS

4. Summary

In conclusion, we have described a simple method for achieving wavelength-tunability in widefield ratiometric fluorescence imaging. Similar to excitation/emission tunable filters, rotating an interference-based dichroic beamsplitter alters its spectral cutoff wavelength. Placing the dichroic beamsplitter in a retroreflector configuration allows for the reflected image to always be directed towards the camera and maintain the optical alignment. We note that optimal tuning of the spectral splitting depends upon the specific spectral properties of the ratiometric indicator, such as the position of the isosbestic point. This configuration may be highly useful in different experimental scenarios where a mixture of heterogeneous fluorescent particles is used for ratiometric imaging, allowing for perfect spectrally balanced detection across a wide field-of-view while using a single dichroic beamsplitter.

Funding

Horizon 2020 Framework Programme (669941).

Acknowledgments

We thank Dov Friedman for machine shop support and Meital Hirshovitz for assisting with cell culture.

Disclosures

The authors declare that there are no conflicts of interest related to this article.

References

1. B. S. Launikonis, J. Zhou, L. Royer, T. R. Shannon, G. Brum, and E. Ríos, "Confocal imaging of [Ca2 +] in cellular organelles by SEER, shifted excitation and emission ratioing of fluorescence," J. Physiol. **567**(2), 523–543 (2005).
2. C. Manno, L. Figueroa, R. Fitts, and E. Ríos, "Confocal imaging of transmembrane voltage by SEER of di-8-ANEPPS," J. Gen. Physiol. **141**(3), 371–387 (2013).
3. S. Farooq and J. Hohlbein, "Camera-based single-molecule FRET detection with improved time resolution," Phys. Chem. Chem. Phys. **17**(41), 27862–27872 (2015).
4. X. Michalet, S. Weiss, and M. Jäger, "Single-molecule fluorescence studies of protein folding and conformational dynamics," Chem. Rev. **106**(5), 1785–1813 (2006).
5. G. S. Harms, M. Sonnleitner, G. J. Schütz, H. J. Gruber, and T. Schmidt, "Single-molecule anisotropy imaging," Biophys. J. **77**(5), 2864–2870 (1999).
6. G. Grynkiewicz, M. Poenie, and R. Y. Tsien, "A new generation of Ca2+ indicators with greatly improved fluorescence properties," J. Biol. Chem. **260**(6), 3440–3450 (1985).
7. E. D. Wieder, H. Hang, and M. H. Fox, "Measurement of Intracellular pH Using Flow Cytometry With Carobxy-SNARF-1," Cytometry **14**(8), 916–921 (1993).
8. A. P. Demchenko, A. S. Klymchenko, V. G. Pivovarenko, and S. Ercelen, "Ratiometric Probes: Design and Applications," in *Fluorescence Spectroscopy, Imaging and Probes*. (Springer, 2002).
9. V. Montana, D. L. Farkas, and L. M. Loew, "Dual-Wavelength Ratiometric Fluorescence Measurements of Membrane Potential," Biochemistry **28**(11), 4536–4539 (1989).
10. S. Jayaraman, J. Biwersi, and A. S. Verkman, "Synthesis and characterization of dual-wavelength Cl−-sensitive fluorescent indicators for ratio imaging," Am. J. Physiol. **276**(3), C747–C757 (1999).
11. H. A. MacLeod, *Thin-Film Optical Filters* (CRC Press, 2010).
12. T. Erdogan, "Optical Filters for Wavelength Selection in Fluorescence Instrumentation," Curr. Protoc. Cytom. **56**(1), 1–25 (2011).
13. P. Favreau, C. Hernandez, A. S. Lindsey, D. F. Alvarez, T. Rich, P. Prabhat, and S. J. Leavesley, "Thin-film tunable filters for hyperspectral fluorescence microscopy," J. Biomed. Opt. **19**(1), 011017 (2013).
14. M. Lequime, "Tunable thin film filters: review and perspectives," Proc. SPIE **5250**, 302–311 (2004).
15. O. Bar-Elli, D. Steinitz, G. Yang, R. Tenne, A. Ludwig, Y. Kuo, A. Triller, S. Weiss, and D. Oron, "Rapid Voltage Sensing with Single Nanorods via the Quantum Confined Stark Effect," ACS Photonics **5**(7), 2860–2867 (2018).
16. T. Parasassi, G. De Stasio, A. d'Ubaldo, and E. Gratton, "Phase fluctuation in phospholipid membranes revealed by Laurdan fluorescence," Biophys. J. **57**(6), 1179–1186 (1990).
17. J. R. Lakowicz, *Principles of Fluorescence Spectroscopy*, 3rd ed. (Springer, 2006).

Biomedical Optics EXPRESS

18. D. M. Owen, C. Rentero, A. Magenau, A. Abu-Siniyeh, and K. Gaus, "Quantitative imaging of membrane lipid order in cells and organisms," Nat. Protoc. **7**(1), 24–35 (2012).
19. K. Park, Z. Deutsch, J. Li, D. Oron, and S. Weiss, "Single Molecule Quantum-Confined Stark Effect Measurements of Semiconductor Nanoparticles at Room Temperatue," ACS Nano **6**(11), 10013–10023 (2012).
20. R. S. Bedlack, M.-d. Wei, and L. M. Loew, "Localized membrane depolarizations and localized calcium influx during electric field-guided neurite growth," Neuron **9**(3), 393–403 (1992).
21. G. Pucihar, T. Kotnik, and D. Miklavčič, "Measuring the Induced Membrane Voltage with Di-8-ANEPPS," J. Visualized Exp. **33**, 1659 (2009).
22. G. Pucihar, T. Kotnik, B. Valič, and D. Miklavčič, "Numerical Determination of Transmembrane Voltage Induced on Irregularly Shaped Cells," Ann. Biomed. Eng. **34**(4), 642–652 (2006).
23. H. P. Schwan, "Electrical Properties of Tissue and Cell Suspensions," Adv. Biol. Med. Phys. **5**, 147–209 (1957).
24. W. Y. Kao, C. E. Davis, Y. I. Kim, and J. M. Beach, "Fluorescence Emission Spectral Shift Measurements of Membrane Potential in Single Cells," Biophys. J. **81**(2), 1163–1170 (2001).
25. A. D. Bachtel, R. A. Gray, J. M. Stohlman, E. B. Bourgeois, A. E. Pollard, and J. M. Rogers, "A Novel Approach to Dual Excitation Ratiometric Optical Mapping of Cardiac Action Potentials With Di-4-ANEPPS Using Pulsed LED Excitation," IEEE Trans. Biomed. Eng. **58**(7), 2120–2126 (2011).